Author Accepted Manuscript, Coastal Engineering, June 2022.
https://doi.org/10.1016/j.coastaleng.2022.104101

Hydrodynamic forces on subsea cables immersed in wave boundary layers

Yunfei Teng[1,2], Terry Griffiths[3], Hongwei An[4], Scott Draper[4], Guoqiang Tang[1,2†], Henning Mohr[3], David J. White[5,2], Antonino Fogliani[4] and Liang Cheng[6]

[1]State Key Laboratory of Coastal and Offshore Engineering, Dalian University of Technology, Dalian, 116024, PR China

[2]International Joint Laboratory on Offshore Oil & Gas Engineering, Dalian University of Technology, Dalian, 116024, PR China

[3]Oceans Graduate School, The University of Western Australia, Crawley, WA 6009, Australia

[4]School of Engineering, The University of Western Australia, Crawley WA 6009, Australia

[5]The University of Southampton, Highfield, Southampton, SO17 1BJ, United Kingdom

[6]Guangzhou International Campus, South China University of Technology, Guangzhou, 511442, PR China

Abstract

This paper investigates the hydrodynamic forces on small-diameter cables (50 mm ≤ D ≤ 200 mm) under wave conditions. A total of 87 experimental tests are conducted in the parameter ranges of $20 \le KC \le 2000$, $10^4 \le Re_p \le 10^5$, $10 \le \beta \le 1000$ and $0.001 < k_s/D \le 2.6$, where KC is the Keulegan–Carpenter number, Re_p is the Reynolds number defined with the cable diameter and peak freestream velocity, β is the Stokes number and $\beta = Re_p/KC$, and k_s/D is the ratio between the seabed roughness and cable diameter. The results show that wave boundary layers significantly affect the forces on cables in contact with the seabed. The variations in the force coefficients with the governing parameters of KC and k_s/D are interpreted based on the characteristic wave boundary layer features, namely, velocity deficit (reduction) and wall turbulence. Two counteracting mechanisms influence the force coefficients: velocity reduction in the wave boundary layers decreases the force coefficients, whereas strong wall turbulence from the seabed increases the force coefficients. Empirical formulas for evaluating the force coefficients of an on-bottom cable immersed in wave boundary layers are proposed based on the present results.

Keywords: *subsea cables, wave boundary layer, hydrodynamic forces, on-bottom stability.*

---

† Email address for correspondence: guoqiang.t@dlut.edu.cn

1 Introduction

With the recent rapid growth of offshore renewable energy, especially offshore wind power, thousands of kilometres of new power transmission cables are laid on ocean floors each year. These cables are sometimes directly laid on the sea floor for various reasons, including the presence of a rocky seabed that precludes cable trenching. The cables are therefore exposed to near-bed flows and need to be designed against a range of metocean conditions, such as waves, tidal currents and combined waves and currents.

DNVGL-RP-F109 (DNVGL, 2021), hereafter referred to as DNV (2021), is one of the prevailing practices for the on-bottom stability design of subsea pipelines. The 'absolute lateral static stability method' recommended by DNV (2021) evaluates the stability of pipelines and cables by comparing the peak hydrodynamic forces induced by extreme flow conditions and the peak resistance provided by the seabed. Using this method, the peak hydrodynamic forces are calculated as follows:

$$\left\{\hat{F}_X, \hat{F}_Z\right\} = \left\{\hat{C}_X, \hat{C}_Z\right\} \times \frac{1}{2}\rho D \hat{U}^2 \tag{1.1}$$

where $\hat{F}_X$ and $\hat{F}_Z$ represent the peak forces per metre in the streamwise and transverse (vertical) directions (N/m), respectively; $\hat{C}_X$ and $\hat{C}_Z$ are the recommended peak force coefficients in the corresponding directions; ρ is the density of the fluid; D is the cable diameter; and $\hat{U}$ is the characteristic velocity. Under wave conditions, DNV (2021) suggests using the peak velocity in the free stream as the characteristic velocity. In DNV (2021), the only governing parameter for the force coefficients under pure wave conditions is the Keulegan–Carpenter number, $KC = \hat{U}T/D$, where T is the wave period. The peak force coefficients $\{\hat{C}_X, \hat{C}_Z\}$ in DNV (2021) are monotonically decreasing functions of KC for $KC \leq 140$, and constant values of $\hat{C}_X = 1.3$ and $\hat{C}_Z = 1.05$ are recommended for $KC > 140$ based on the underlying pipe hydrodynamics research reported in DHI (1986).

Since most of the existing on-bottom stability design methods, including the absolute lateral static stability method suggested by DNV (2021), were developed for relatively large-dimeter oil and gas pipelines, they are not necessarily directly applicable to small-diameter power cables. Compared to pipelines, subsea cables have the following typical characteristics that may affect the hydrodynamic forces:

- The diameter of a typical power transmission cable is within a range of 50 mm to 200 mm, which is relatively small compared with the diameter of a typical oil and gas pipeline, which ranges from 200 mm to 1200 mm.
- Offshore renewable energy projects are preferentially located in areas of strong wind, wave or tidal current energy. Accordingly, the power cables used to support these projects often experience more severe design conditions than those used for oil and gas pipelines. Under extreme wave conditions, KC can reach $O(10^3)$; in these conditions, the cables are expected to be immersed in the wave boundary layers (WBLs) and to experience significant velocity reductions.
- The seabed roughness k_s to cable diameter D ranges up to $k_s/D = O(10)$ for cables crossing a

rocky seabed. A greater seabed roughness leads to a thicker WBL and stronger wall turbulence (e.g., Jonsson & Carlsen 1976, Sleath 1987, Jensen et al. 1989, Dixen et al. 2008, Yuan & Madsen 2014, Teng et al. 2021) to which power cables are exposed.

The velocity reduction due to WBL and the enhanced wall turbulence due to seabed roughness may affect the hydrodynamic forces on a small-diameter cable. Cheng et al. (2016) demonstrated through an analytical approach and Tang et al. (2018) demonstrated through a numerical investigation that ignoring the velocity reduction due to the WBLs is overly conservative for the on-bottom stability design of small cables. Tang et al. (2018) showed that the velocity reduction in the WBLs potentially causes up to a 40% reduction in the required stable weight at KC = 450. Tang et al. (2018) also found that seabed roughness leads to an almost linear reduction in force coefficients with increasing k_s/D at $k_s/D > 0.05$.

Given the above observations, a sound understanding of wave-induced hydrodynamic forces on small-diameter power cables could lead to reduced lifecycle costs, increasing the competitiveness of offshore renewable energy.

Although numerous investigations into the hydrodynamics acting on a cylinder have been conducted in the past decades, only a few of them provide datasets with an on-bottom setup (i.e., no gap between the model seabed and the cylinder) and under wave conditions, e.g., Sarpkaya & Rajabi (1976), DHI (1986) and DNV (2021). In these publications, the upper limit of KC was approximately 100~200. The upper limit of KC that Tang et al. (2018) used was 450. The upper limit of k_s/D that DHI (1986) and Tang et al. (2018) used was 0.05 and 0.2, respectively. As mentioned above, for a small-diameter power cable, the KC number can be on the order of $O(10^3)$, and the value of k_s/D can be up to $O(10)$. Therefore, despite the invaluable insights from existing studies, more experimental data are required for higher KC and k_s/D conditions. In addition, the effect of the Reynolds number ($Re_p = \hat{U}D/\nu$) should be considered, where ν is the kinematic viscosity of the fluid. The experimental study described in this paper addresses these knowledge gaps.

The remainder of this paper is organized as follows: the experimental setup is described in §2; a validation of the present measurements is conducted in §3; the results and discussions are presented in §4; prediction methods are suggested in §5; and the conclusions are drawn in §6. More detail on the validation of the force measurement is provided in the supplementary document.

2 Physical model tests

2.1 The O-tube facility, cable model and seabed model

Physical experiments were conducted in a recirculating water flume (O-tube) in the Coastal and Offshore Engineering Laboratory (COEL) of the University of Western Australia. The oscillatory wave velocities were generated by an axial flow impellor pump driven by a variable-frequency multi-pole electric motor, as described in a number of publications (e.g., An et al. 2013, White et al. 2014, Leckie et al. 2015, Zhang et al. 2017, Yang et al. 2018, Griffiths et al. 2018 & 2019) that demonstrate the capabilities and effectiveness of the O-tube facility in modelling a range of practical problems related to the on-bottom stability of subsea cables / pipelines. The size of the O-tube test section is 17.4 m in length, 1 m in height (above the false floor) and 1 m in width. Given that the O-tube facility is fully enclosed without a free surface, oscillatory flows were used to simulate waves induced near seabed flows. The motor and control system enable the generation of regular waves, irregular waves, steady currents, or combined wave and current conditions. While tests with irregular waves and tests with combined wave and current conditions have been undertaken as part of a larger project (see Griffiths et al. 2019), this work reports the findings of the regular wave (sinusoidally oscillatory flow) tests.

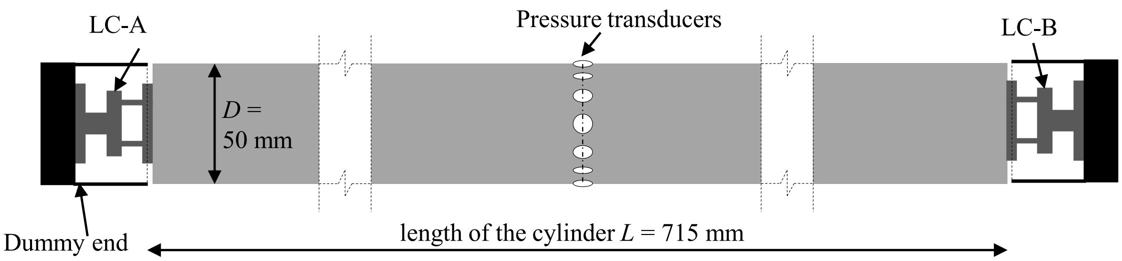

Figure 1. Sketch of the model cable.

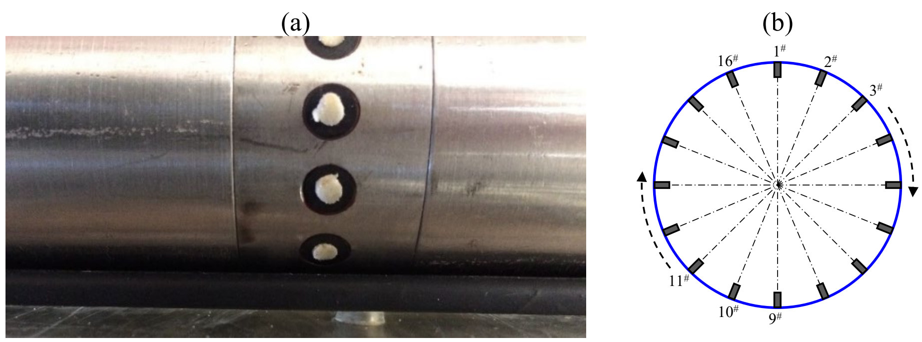

Figure 2. (a) Close-up photograph and (b) schematic arrangement of PTs.

The power cable was modelled by a cylinder with an external diameter of D = 50 mm and a length of L = 715 mm, as sketched in Figure 1. Each end of the cylinder features a dummy end-section within which a bi-axial load cell (LC) was installed to measure the hydrodynamic forces on the test section of the cylinder in the streamwise (x) and transverse (z) directions. The surface of the cylinder was smoothly milled stainless steel, which was regularly cleaned during the extended testing program. The total streamwise force was calculated by summing the measurements recorded by the two LCs. A total of 16 equally spaced pressure transducers (PTs) were installed circumferentially around the cylinder at its mid-span. A close-up photograph and a sketch of the arrangement of the PTs are shown in Figure 2. All the measured data were logged simultaneously using the University of Western Australia (UWA)'s digital data logging system 'DigiDaq' described by Gaudin et al. (2009). The instantaneous water pressure measured around the cylinder circumference by using the m-th PT is denoted as p_m, and its direction is starting from the position of the m-th PT and pointing to the axis of the circular cross section. Its horizontal and vertical components are added to the total streamwise and transverse forces, respectively. The streamwise and transverse forces per unit length can be calculated through the integral operations specified as follows,

$$F_X = -\sum_{m=1}^{16} p_m \sin\left(\frac{m-1}{8}\pi\right)\cdot\frac{\pi D}{16}, \tag{2.1}$$

$$F_Z = -\sum_{m=1}^{16} p_m \cos\left(\frac{m-1}{8}\pi\right)\cdot\frac{\pi D}{16}, \tag{2.2}$$

where F_X and F_Z represent the desired hydrodynamic forces per metre in the streamwise and transverse directions, respectively.

Table 1. Information on the seabed models.

Seabed model	Description	Elements	Size of elements	Roughness k_s (mm)	k_s/D	Arrangement
PLN	plane	plane false floor	O(1 μm)	O(0.1)	$O(10^{-3})$	--
SND	coarse sand	sandpaper	1.3 mm	4	0.08	scattered
TTB	rocky	concrete spheres	38 mm	130	2.6	rectangular

Figure 3. Close-up photographs for SND (for sand bed, in the left) and TTB (for table-tennis-ball bed, in the right) seabed models.

Three seabed models, which have been described previously by Griffiths et al. (2019), were used to represent a range of seabed roughness conditions, representing flat, coarse sand and rocky seabed conditions. Table 1 lists details of the three seabed models, which are denoted as follows: PLN was the plane false floor, while SND and TTB had floor coverings of (a) sandpaper with a medium particle size of d_{50} = 1.3 mm and (b) a regular array of interconnected concrete spheres with d_{50} = 38 mm (the spheres covering the whole false floor have the same diameter), respectively. The Nikuradse equivalent sand roughness k_s was determined from the logarithmic law fitted to the velocity profile (at the phase when the freestream velocity is the maximum) in the logarithmic region. Figure 3 shows close-up photographs of the SND and TTB seabed models. The seabed models occupied the full length and width of the flume, resulting in an upstream 'fetch' of approximately 8.7 m, over which the applied flow was able to generate a mature and evolved boundary layer profile.

In the present tests, the cylinder was laid on the seabed model, and the gap between them was sealed. Similar to the seal arrangement adopted by Sarpkaya & Rajabi (1979), a flexible double-layer plastic 'foil' was secured under the cylinder, with one layer sticked to the cylinder and the other sticked to the false floor. The gap has a height of 0.5 mm and the double-layer foil has a thickness of 0.3 mm. The seal prevents flow under the cylinder while transmitting only small extraneous streamwise or transverse forces into the LC measurements. Calibrations on the effect of the seal are provided in the supplementary document, §S1. Specially, under TTB conditions, the gaps between the cylinder and the spheres were sealed. With this setup the hydrodynamic forces are expected to feel the effect of WBL developed from the rough wall in the upstream, but not feel the effect of the interaction between the cylinder and the spherical roughness elements. The origin of the vertical coordinate $z = 0$ was set at the top of the rectangular box which is as high as the crest of the roughness elements.

2.2 Velocity measurements

The free stream velocity was measured by a Nortek Vectrino-II Acoustic Doppler Velocimeter (ADV) located in the centre of the flume and 360 mm above the false floor, as sketched in Figure 4. As the primary focus of this work is the determination of hydrodynamic force coefficients with the freestream velocity, the ADV velocity measurements and the LC force measurement are recorded simultaneously.

To acquire detail WBL information, the velocity field in the *o-x-z* plane was measured by a two-dimensional particle image velocimetry (PIV) in the absence of the cylinder, as sketched in Figure 4. The measurement zone was set in the middle of the test section and across the midline in the longitudinal direction of the flume. A Class-4 green continuous laser (MicroVec SM-SEMI-5W LWGL532 083298 5W 513 nm) was used to illuminate the flow. The laser sheet was projected vertically down through a 30° fan angle cylindrical lens and a rectangular glass bucket. The glass bucket was used to ensure that the laser sheet was not disturbed by air bubbles trapped below the lid. The glass bucket was inserted into the flume through a slot cut in the centre of the lid of the test section, and this bucket was sufficiently small and far from the zone of interest. The flow was seeded with Rilsan D60 NAT fine polyamide particles with a mean diameter of 40~45 μm, specific density of 1.04 and seeding density of 0.5 ppm by mass, so approximately 6 particles were visible per cm^2 in the illuminated laser sheet. A Photron SA3 high-speed digital camera (1024 × 1024 pixels) was used to capture the flow image. The camera was positioned to capture as much of the vertical boundary layer above the seabed models as possible while maintaining the required image resolution (0.36 mm/pixel). For all the tests, the near-bed flow in a zone of approximately 0.12 m × 0.37 m (width × height) was well illuminated and captured by the camera. During the image collection, 90~110 image pairs at a single phase were available for the ensemble average. The time interval in each image pair ranged from 1 ms to 4 ms. Assuming the correlation peak displacement was identified to an accuracy of 0.1 pixels, cf. Westergaard et al. (2003), the velocity was accurate to a maximum resolution of 0.9 cm/s and a minimum of 3.6 cm/s.

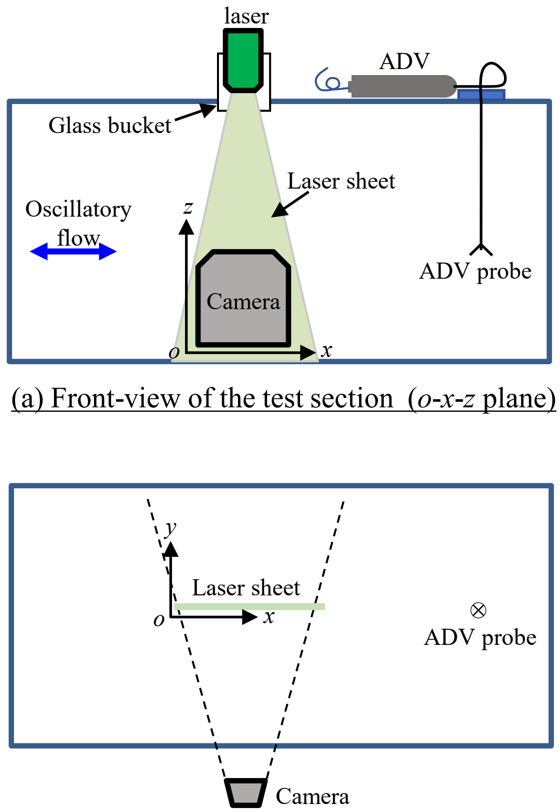

(a) Front-view of the test section (o-x-z plane)

(b) Top-view of the test section (o-x-y plane)

Figure 4. Sketch of the PIV and ADV setups.

The image analysis was conducted by using the open-source program 'PIVlab' on the MATLAB platform, cf. Thielicke & Stamhuis (2014a, 2014b) and Thielicke (2014). The well-illuminated area of each image was used as the zone of interest. The fast Fourier transform (FFT) window deformation algorithm was adopted for the cross-correlation analysis. The interrogation area was set as 64 × 64 pixels with 75% overlap in the first iteration and 32 × 32 pixels with 50% overlap in the second iteration. Erroneous flow vectors were detected by (*i*) comparing the vectors with the prescribed velocity limit and (*ii*) using a standard deviation filter with the threshold set to 7 times the standard deviation. The erroneous and missing vectors (less than 3% of the total number of vectors) were replaced with their local mean vectors.

The double-averaged velocity was obtained through ensemble averaging over 90~110 image pairs at each phase angle and spatial averaging over 15~20 adjacent x-positions (in the streamwise direction):

$$\tilde{u}(z,t) = \frac{1}{KQ}\sum_{k=1}^{K}\sum_{q=1}^{Q} u\left(x_k, z, t+(q-1)T\right), \quad 0 \le t < T, \tag{2.3}$$

where u is the streamwise velocity, the '~' sign represents the double-averaging operation, t is the time, K is the total number of x-positions used for spatial averaging and Q is the total number of image pairs at a given phase used for ensemble averaging. The starting phase $\omega t = 0$ is defined as the phase when the free stream velocity is the maximum. Here, ω is the angular frequency $\omega = 2\pi/T$. The double-averaged free-stream velocity is referred to as $\tilde{U}$, and its peak value is denoted as U_w. The deviation of U_w measured by the ADV (at z = 360 mm) and PIV (at z = 300 mm) is smaller than 1.3%. The velocity fluctuation was calculated by

$$u'(x,z,t) = u(x,z,t) - \tilde{u}(z,t) \tag{2.4}$$

and the double-averaged turbulence intensity $\sqrt{\widetilde{u'^2}}$ was calculated by

$$\sqrt{\widetilde{u'^2}}(z,t) = \sqrt{\frac{1}{KQ}\sum_{k=1}^{K}\sum_{q=1}^{Q} u'^2\left(x_k, z, t+(q-1)T\right)}, \quad 0 \le t < T\ . \tag{2.5}$$

2.2 Test matrix

A total of 29 sinusoidal oscillatory flow tests were conducted under each seabed roughness condition, together with four unidirectional flow tests for validation purposes. Table 2 lists the details of these tests, where U_w represents the peak velocity in the freestream under oscillatory flow (wave) conditions and U_c represents the time-averaged velocity in the freestream under unidirectional flow (current) conditions. The flow ID indicates the approximate values of KC and U_w or U_c. Figure 5 shows the parameter space covered by the present and published tests. Besides, the present tests extended the available parametric range of k_s/D to 0.001 to 2.6. The ranges of a/k_s are: 10^4~10^5 for the PLN tests, 60~3000 for the SND tests and 2~120 for the TTB tests, where a is the semi-excursion in the free stream, defined as $a = U_wT/(2\pi)$.

Table 2. Flow conditions reported in this work (ADV velocity measurements at 360 mm above the PLN bottom are used to determine U_w, U_c and T).

Flow ID	U_w (m/s)	T (s)	Flow ID	U_w (m/s)	T (s)
KC20Uw020	0.20	5.38	KC200Uw100	0.96	10.88
KC40Uw020	0.20	10.49	KC500Uw050	0.46	53.53
KC40Uw030	0.30	7.27	KC500Uw100	0.94	27.00
KC40Uw040	0.41	5.40	KC500Uw150	1.43	18.18
KC40Uw050	0.50	4.34	KC1000Uw050	0.47	107.13
KC60Uw020	0.22	16.00	KC1000Uw100	0.92	53.53
KC60Uw030	0.30	10.76	KC1000Uw150	1.42	35.09
KC60Uw040	0.39	7.35	KC1000Uw200	1.88	27.03
KC60Uw050	0.50	6.31	KC2000Uw050	0.50	216.60
KC60Uw060	0.62	5.37	KC2000Uw100	0.97	108.16
KC80Uw020	0.21	21.50	KC2000Uw150	1.46	73.05
KC80Uw030	0.29	13.78	KC2000Uw200	1.91	53.67
KC80Uw040	0.42	10.69	Flow ID	U_c (m/s)	
KC80Uw050	0.51	8.38	Uc050	0.49	
KC80Uw060	0.60	7.45	Uc100	0.97	
KC100Uw050	0.50	10.68	Uc150	1.43	

KC200Uw050	0.47	21.69	Uc200	1.91

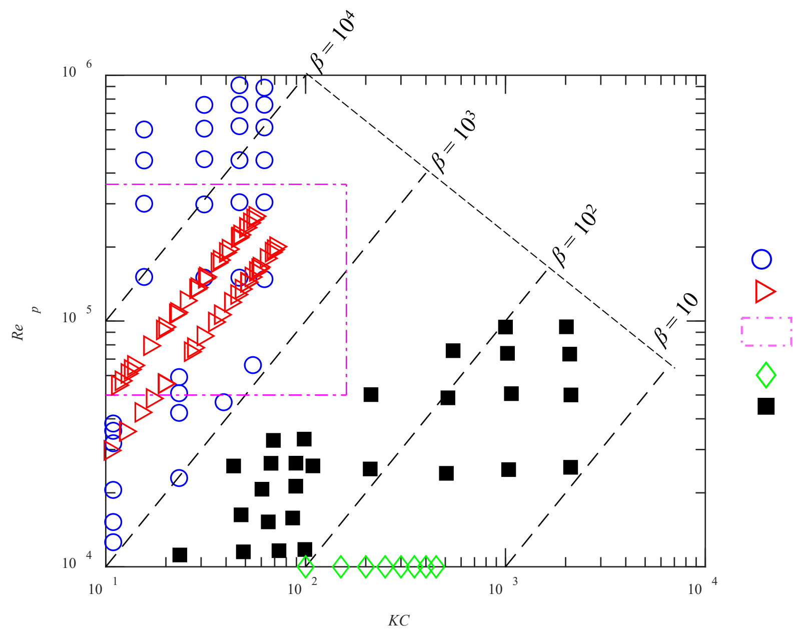

Figure 5. Parameter range for the present measurements and those available in the literature. β is the Stokes number representing the quotient of Re_p over KC, namely, $\beta = Re_p/KC$. In Yamamoto & Nath's (1976) tests, two cylinders with diameters of 0.30 m and 0.0762 m were used, and the smallest gap-to-diameter ratio were 0.083 and 0.063, respectively.

2.3 Post-processing

Under wave conditions, the forces were ensemble-averaged to determine the force coefficients,

$$\tilde{F}_i(t) = \frac{1}{N}\sum_{n=1}^{N} F_i\left(t + (n-1)T\right), \quad 0 \le t < T, \tag{2.6}$$

where N ($\geq$ 20) is the number of wave cycles, F_i represents the force in either horizontal and vertical directions, namely F_X or F_Z. The start of the test cycle $t = 0$ was synchronized with the time when the free stream velocity $\tilde{U}(t)$ was the maximum. The peak value of $\tilde{F}_i$ in a flow cycle is referred to as $\hat{F}_i$, where the '^' sign represents the peak of the ensemble-averaged force. The peak coefficients $\hat{C}_i$ corresponding to the peak forces $\hat{F}_i$ were defined as

$$\hat{C}_i = \hat{F}_i \Big/ \left(\frac{1}{2}\rho D U_w^2 L\right). \tag{2.7}$$

The Morison-type force coefficients $\{C_D, C_M\}$ were fitted using a least-square optimization from the following correlation between $\tilde{F}_X(t)$ and freestream velocity $\tilde{U}(t)$:

$$\tilde{F}_X = \frac{1}{2}\rho D C_D \tilde{U}\left|\tilde{U}\right| + \frac{1}{4}\rho\pi D^2 C_M \frac{\partial \tilde{U}}{\partial t}, \tag{2.8}$$

where C_D and C_M are the coefficients corresponding to the drag and inertia forces, respectively.

Under current conditions, a time-averaging process was specified as

$$\overline{F}_i = \frac{1}{M}\sum_{m=1}^{M} F_i\left(t + m\Delta t\right), \tag{2.9}$$

where M is the total sample number of the measured force, Δt is the time interval of the record, and the '–' sign represents the time-averaging process. The mean force coefficients $\overline{C}_i$ normalized by the free stream velocity were written as

$$\overline{C}_i = \overline{F}_i \Big/ \left(\frac{1}{2}\rho D U_c^2 L\right). \tag{2.10}$$

3 Validation tests

To ensure the reliability of the present measurements, the test results under PLN conditions (a smooth and plane bed) were examined. The results measured by LC and PT were compared with those reported in the literature, as provided in the supplementary document, §S2. The peak force coefficients measured by LC are smaller than those measured by PT. This behaviour is explained based on the physics revealed in Sumer and Fredsøe (2006, p28-32). The vortex shedding occurs in cells along the length of the cylinder. The averaging force acting on the cylinder over the whole length, which is measured by LC, is smaller than the averaging force over the length of the cell of vortex shedding, which is measured by PT. In the present range of Re_p, the correlation length of the cell of vortex shedding is approximate to $(2 \sim 3)D$, based on the work reported by Gerlach and Dodge (1970). In general, the LC measurements agree better with the results reported in literature in terms of the peak force coefficients, whereas the PT measurements agree better with the literature in terms of the root-mean-square force coefficients. As the peak forces are the focus of the present study, LC measurements were used in the following analysis.

The comparisons between the present results (measured by LCs) and the literature under wave conditions are presented below. As the existing datasets concerning the on-bottom cylinders ($G = 0$) are relatively rare, as shown in Figure 5, validations against existing datasets with similar ranges of governing parameters (KC, Re_p) are not possible. Since KC is the primary parameter of concern in the present study, we relaxed the requirement of matching the range of Re_p during the validations. The effect of Re_p at a constant KC will be discussed later on.

Figure 6 compares the present results with those reported by Sarpkaya & Rajabi (1979) and DHI (1986). The ranges of Re_p shown in Figure 6 are $(10\sim11) \times 10^4$, $(5\sim36) \times 10^4$ and $(1\sim10) \times 10^4$ for the datasets of Sarpkaya & Rajabi (1979), DHI (1986) and the present study, respectively. Figure 6 shows that the present results are larger than the earlier results. Further examinations show that the present C_D and C_M are approximately 1.1 and 1.3 times those reported by DHI (1986), respectively. This discrepancy is attributed to the influence of Re_p. To support the above claim, the variation trend of C_D with Re_p is discussed. Figure 7 presents the results of C_D (plane bottom tests, measured by LCs) obtained from the present study and the literature as a function of Re_p at similar KC numbers. Since few data are available for an on-bottom geometry (G = 0), the data with a small gap (G = 0.063 and 0.083) obtained from Yamamoto & Nath (1976) are also compared. Although C_D generally varies with respect to Re_p, the ratio between the standard deviation and the average on the order of 20% may be attributed to different setups of the gap. This is also evidenced by the results provided in the supplementary document, §S1.

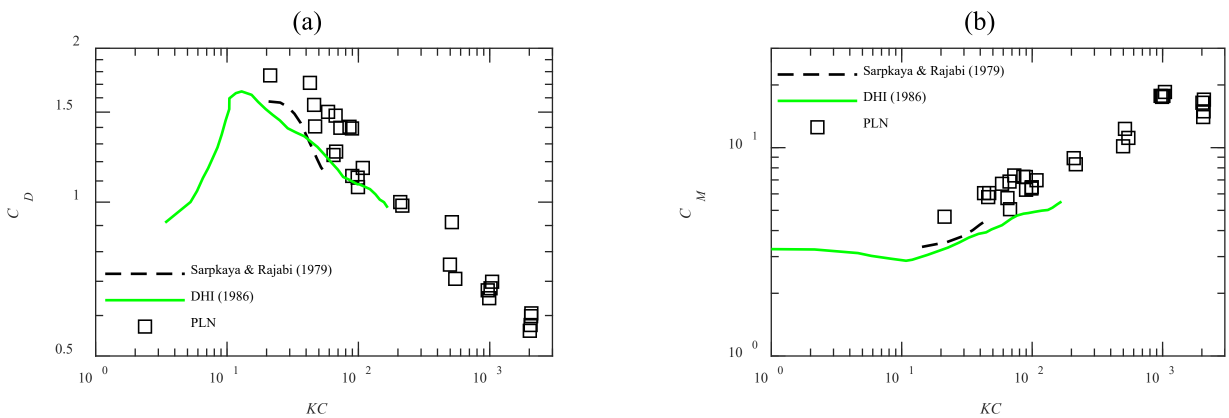

Figure 6. (a) C_D and (b) C_M vs. KC based on the PLN tests. $Re_p = (10\sim11) \times 10^4$ in the work of Sarpkaya & Rajabi (1979), $Re_p = (5\sim36) \times 10^4$ in the work of DHI (1986), and $Re_p = (1\sim10) \times 10^4$ in the present tests. The data of Sarpkaya & Rajabi (1979) are taken from Sumer et al. (1991) and Sumer & Fredsøe (2006, p181).

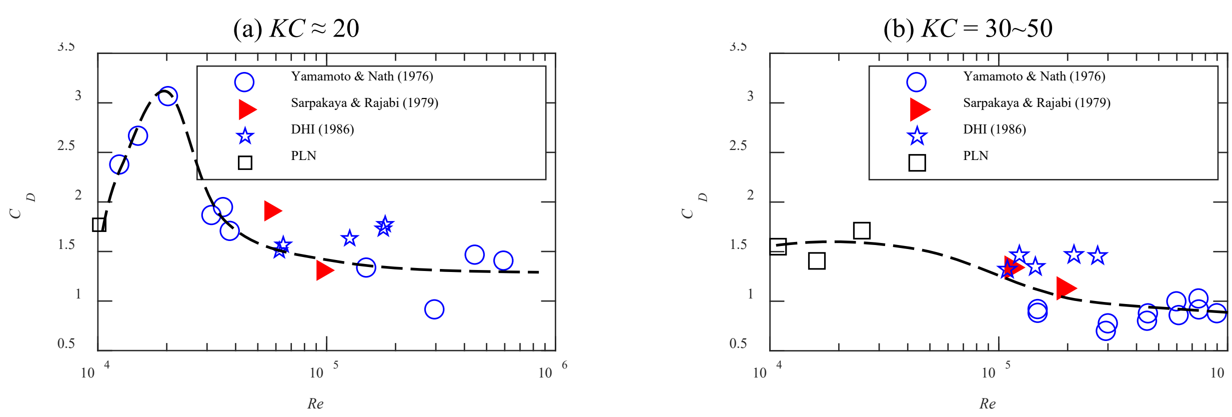

Figure 7. C_D vs. Re_p at similar KC numbers, obtained from plane bottom tests in the present work and available literature. For the data acquired from Yamamoto & Nath (1976), in (a), $KC \in [11, 24]$, G = 0.063 and 0.083; in (b), $KC \in [31, 47]$, G = 0.083.

Figure 8 compares the peak force coefficients $\{\hat{C}_X, \hat{C}_Z\}$ based on the present PLN measurements with those reported by DNV (2021), DHI (1986) and Tang et al. (2018). In the range of $KC < 140$, the present results are slightly larger than the DNV (2021) recommendation due to the different Re_p values investigated in those studies. In the range of $KC \geq 140$, the present results agree reasonably well with those reported by Tang et al. (2018) and are notably smaller than the constant values recommended by DNV (2021), $\{\hat{C}_X, \hat{C}_Z\} = \{1.30, 1.05\}$. In the present study and the work of Tang et al. (2018), the diameter of the cylinder is smaller than or comparable to the thickness of WBLs; hence, the flow velocity reduction in the WBLs reduces the hydrodynamic forces significantly, as shown in Figure 8. However, this effect cannot be considered in DNV (2021), resulting in conservative forces and the resultant on-bottom stability design for cables (or small-diameter pipelines). In addition, the present data, shown in Figure 8, are scattered at a constant *KC* number, which is attributed to the different Re_p numbers.

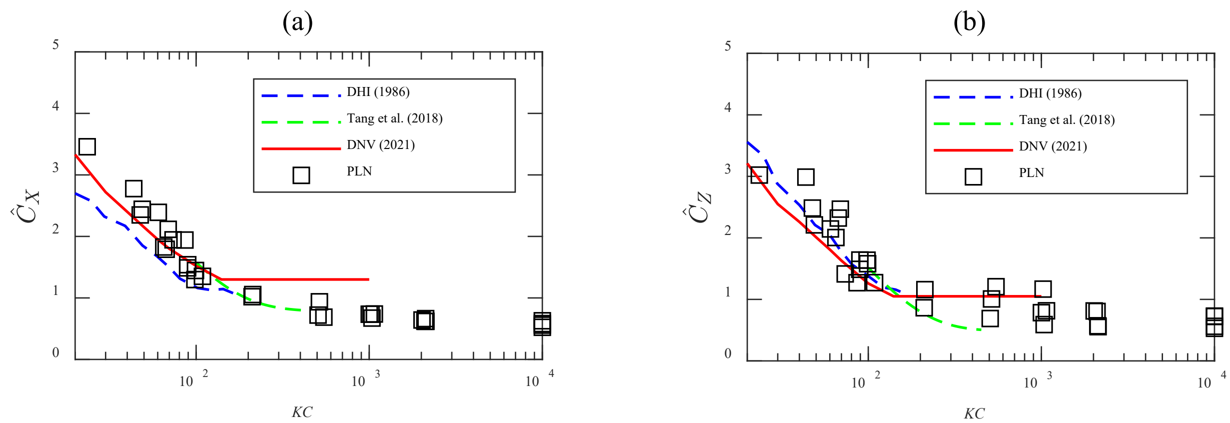

Figure 8. Comparison between the present measurements and the results reported in the literature: (a) $\hat{C}_X$ vs. *KC*; (b) $\hat{C}_Z$ vs. *KC*. The results of steady current tests are shown in the figure at $KC = 10^4$.

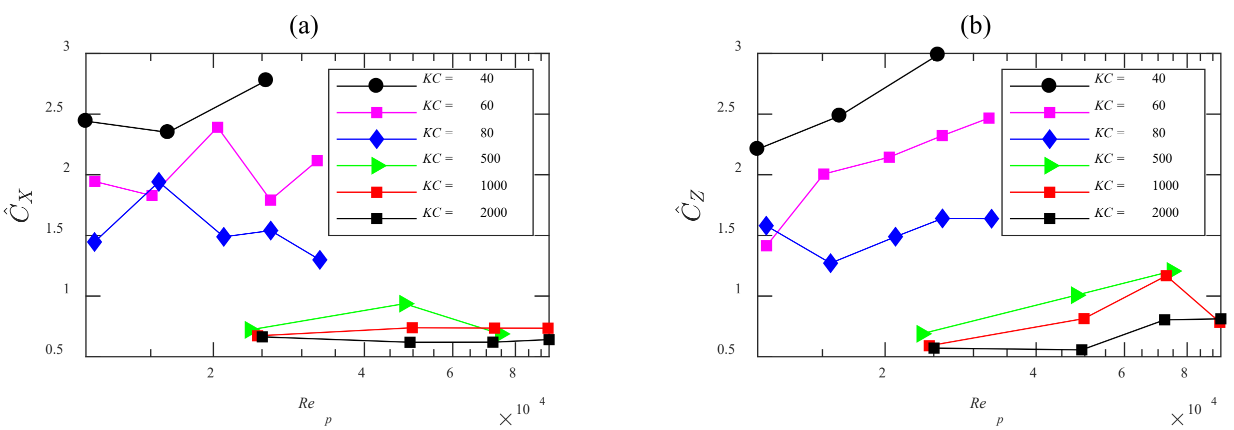

Figure 9. The effect of Re_p on peak force coefficients (a) $\hat{C}_X$ and (b) $\hat{C}_Z$, based on the present PLN measurements.

Figure 9 presents the peak force coefficients obtained from the present PLN tests as functions of Re_p at various *KC* numbers. Although general variation trends of $\{\hat{C}_X, \hat{C}_Z\}$ with Re_p are observed, albeit with notable scatter, it might be not necessary to describe these trends as quantitative functions, given the small range of Re_p investigated in the present study. The variations in peak force coefficients over $Re_p = 10^4 \sim 10^5$

are treated as scatter and quantified by their standard deviations in the following discussions. Additional validations based on steady current results are provided in §S3.

4 Results and discussions

4.1 Test results

Figure 10 presents the peak force coefficients $\{\hat{C}_X, \hat{C}_Z\}$ obtained from three kinds of seabed conditions. The parameter ranges of the present experiments are $20 \leq KC \leq 2000$, $10^4 \leq Re_p \leq 10^5$, $10 \leq \beta \leq 1000$ and $10^{-3} \leq k_s/D \leq 2.6$. The scatter in the data with respect to different Re_p at identical KC and k_s/D are represented by their standard deviations, which are presented as error bars in Figure 10. The $\{\hat{C}_X, \hat{C}_Z\}$ obtained under steady current conditions are presented at $KC = 10^4$ in Figure 10.

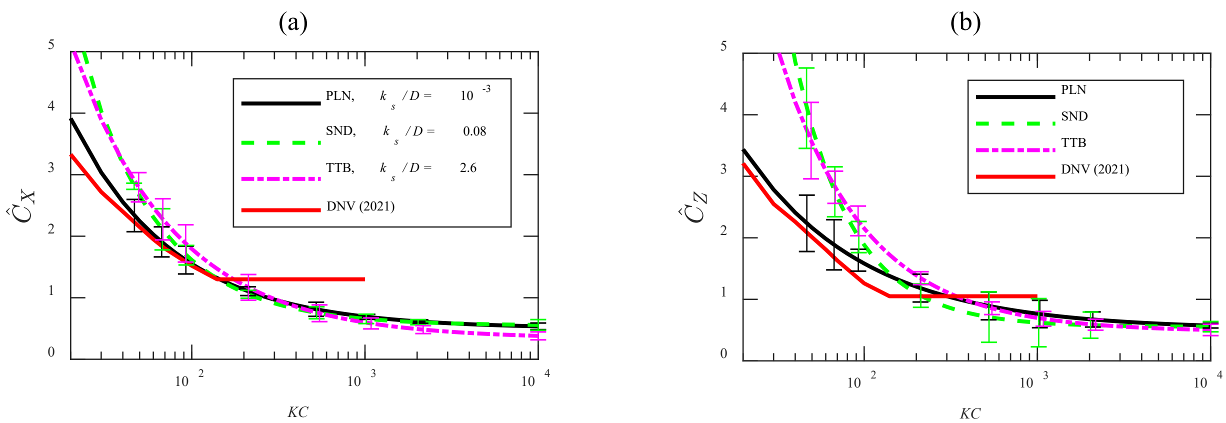

Figure 10. Force coefficients (a) $\hat{C}_X$ and (b) $\hat{C}_Z$ vs. KC obtained from tests under different seabed conditions. The steady current results are shown at $KC = 10^4$. The characteristic velocity is the peak velocity in the free stream.

The following features were observed. (i) The present PLN results are notably smaller than the DNV (2021) recommendations at large KC numbers. (ii) Compared to the PLN results, a larger k_s/D leads to higher force coefficients at small KC numbers but lower force coefficients at large KC numbers. These two features are discussed below.

4.2 Variation of peak force coefficients with *KC*

Concentrating on the PLN results, the variation trend of the force coefficients with KC is discussed here. Compared to DNV (2021) recommendations, the smaller $\{\hat{C}_X, \hat{C}_Z\}$ values at larger KC numbers ($\geq$ 200) are attributed to greater velocity reductions in the WBLs with increasing KC number. The profiles of velocity amplitude in the WBLs, acquired from PIV measurements in the absence of the cylinder, are shown in Figure 11 for PLN tests with various KC numbers at a fixed $Re_p \approx 2.5 \times 10^4$. The greater velocity reduction for a larger KC number is due to the increase in WBL thickness. This point is further elaborated below.

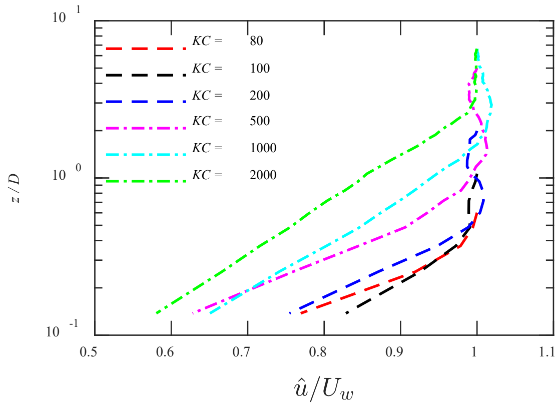

Figure 11. Profiles of velocity amplitude in the WBLs at various KC numbers and $Re_p \approx 2.5 \times 10^4$ under PLN conditions.

The WBL thickness δ_J can be estimated from available empirical formulas that are functions of a/k_s. Here, δ_J is defined as the elevation of the maximum velocity overshoot in the WBL (Jensen et al. 1989), and a is the free stream semi-excursion of fluid particles. For example, the formula suggested by Dixen et al. (2008) is written as

$$\frac{\delta_J}{k_s} = 0.08\left(\frac{a}{k_s}\right)^{0.82} + 0.08,\ \ 0.5 \le a/k_s \le 5000. \tag{4.1}$$

Substituting $a = KC \cdot D/(2\pi)$ into eq. (4.1) results in the following formula:

$$\frac{\delta_J}{D} = 0.0177KC^{0.82}\left(\frac{k_s}{D}\right)^{0.18} + 0.08\frac{k_s}{D}. \tag{4.2}$$

Eq. (4.2) shows that δ_J/D increases with KC and k_s/D, leading to greater velocity reductions in the WBLs. The greater velocity reductions in turn result in greater reductions in the hydrodynamic forces and force coefficients (because the force coefficients are normalized by the free stream velocity).

To further substantiate the above interpretations of the decreasing $\{\hat{C}_X, \hat{C}_Z\}$ with increasing KC ($KC \ge 200$), the force coefficients are normalized by the cross-sectional average peak velocity U_{wp}. The modified set of peak force coefficients, referred to as $\hat{C}_i'$, are written as

$$\hat{C}_i' = \hat{F}_i \Big/ \left(\frac{1}{2}\rho D U_{wp}^2 L\right). \tag{4.3}$$

If the greater velocity reductions are indeed the causes for the observed variation trends of $\{\hat{C}_X, \hat{C}_Z\}$ with KC, the modified set of peak force coefficients would be less dependent on KC at large KC values. For clarity, the parameters with a prime, e.g., Re_p', KC', $\overline{C}_i'$ and $\hat{C}_i'$, hereafter, represent normalizations by the local average velocity across the cylinder.

Figure 12 examines the modified set of peak coefficients $\{\hat{C}_X', \hat{C}_Z'\}$ under PLN seabed conditions at a constant Re_p (Re_p' deviates slightly). The original set of peak force coefficients $\{\hat{C}_X, \hat{C}_Z\}$ and the force coefficients recommended by DNV (2021) are also presented in Figure 12 for comparison. The modified set is approximately constant at large KC numbers (≥ 200) and close to the DNV (2021) recommendation. This confirms that the decreasing trend of the force coefficients $\{\hat{C}_X, \hat{C}_Z\}$ with increasing KC at large KC numbers is primarily due to the velocity reductions in the WBLs.

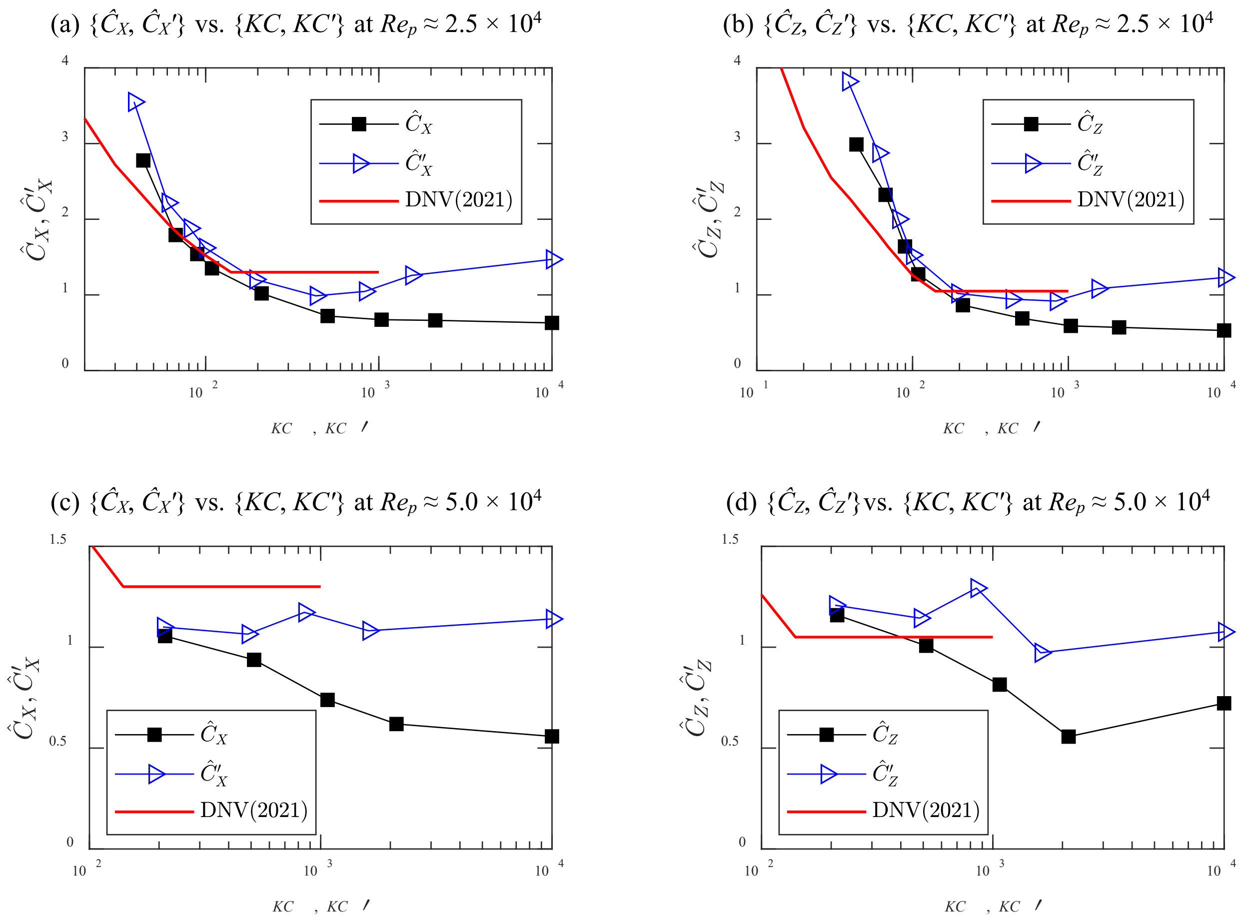

Figure 12. Comparison between two sets of peak force coefficients, based on PLN results. The steady current results are shown at $\{KC, KC'\} = 10^4$.

Other representations of local velocity have been examined to normalize the forces; see further details in §S4. It was found that the peak force coefficients normalized by the average velocity across the cylinder and by the velocity at the axis of the cylinder collapse to a single trend for different KC numbers. However, to match the option suggested by DNV (2021) under current conditions, the cross-sectional average peak velocity was adopted in the present study.

4.3 Variation in peak force coefficients with k_s/D

As identified in eq. (4.2), a rougher seabed (i.e., larger k_s/D) also leads to an increased WBL thickness and therefore greater velocity reduction, from which a reduction in the force coefficients $\{\hat{C}_X, \hat{C}_Z\}$ might be expected. However, as shown in Figure 10, a larger k_s/D leads to greater force coefficients for $KC \leq 200$. These behaviours are explained below.

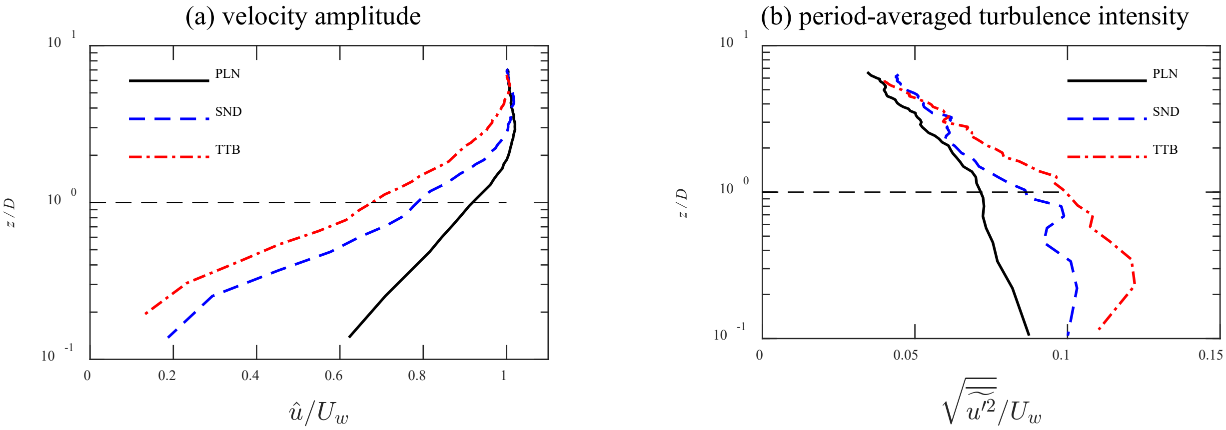

Figure 13. (a) Velocity amplitude profiles and (b) period-averaged turbulence intensity profiles obtained from PLN, SND and TTB tests, with $KC \approx 1000$ and $Re_p \approx 2.5 \times 10^4$. The black dashed line represents the top of the cylinder.

It is known that a greater seabed roughness leads to more violent wall turbulence (Sleath 1987, Jensen et al. 1989, van der A et al. 2011, Milne et al. 2013a, Milne 2013b, Mercier et al. 2021, Milne et al. 2021), which will affect the boundary layer transition and flow separation around the cylinder and the resultant force coefficients (Cheung & Melbourne 1983, Sumer & Fredsøe 2006). Figure 13 shows examples of velocity reduction and turbulence profiles obtained from tests with different k_s/D values at identical KC and Re_p numbers. It is demonstrated in §4.1 that the effect of velocity reduction can be largely eliminated by normalizing the force with the cross-sectional average velocity, namely using the modified set of peak force coefficients $\{\hat{C}_X', \hat{C}_Z'\}$ as shown in Figure 12. Therefore, the contribution of wall turbulence can be distinguished by comparing the modified set of peak force coefficients $\{\hat{C}_X', \hat{C}_Z'\}$ obtained from tests under different seabed conditions.

Figure 14 presents the modified set of peak force coefficients $\{\hat{C}_X', \hat{C}_Z'\}$ as a function of KC' obtained from tests under different k_s/D values and a similar Re_p. A greater seabed roughness leads to larger force coefficients of $\{\hat{C}_X', \hat{C}_Z'\}$ over the whole KC' range, and the wave results at high KC' numbers approximate the steady current results. This behaviour indicates that the wall turbulence affects the force coefficients under wave and current conditions in a similar way. As a result, we further interpreted the effect of turbulence by extending the approach used for current alone.

(a) $\hat{C}_X'$ vs. KC' at $Re_p \approx 2.5 \times 10^4$

(b) $\hat{C}_Z'$ vs. KC' at $Re_p \approx 2.5 \times 10^4$

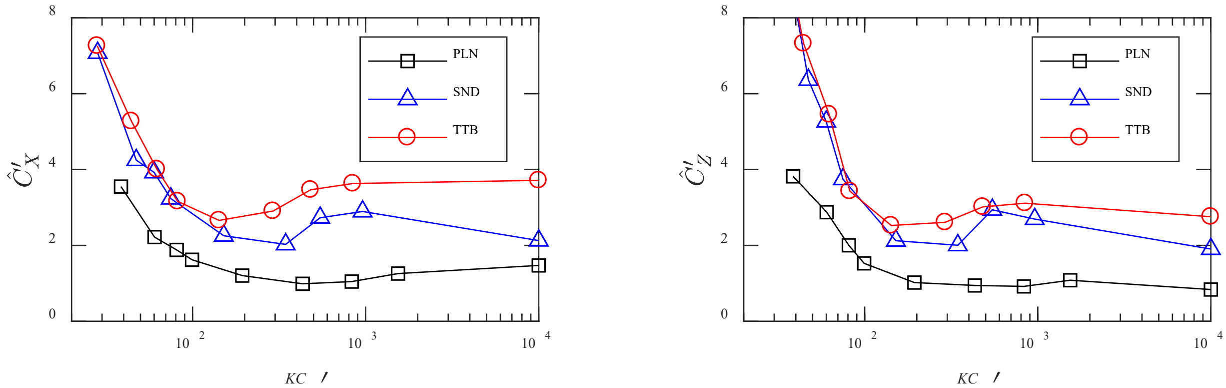

(c) $\hat{C}_X'$ vs. KC' at $Re_p \approx 5 \times 10^4$

(d) $\hat{C}_Z'$ vs. KC' at $Re_p \approx 5 \times 10^4$

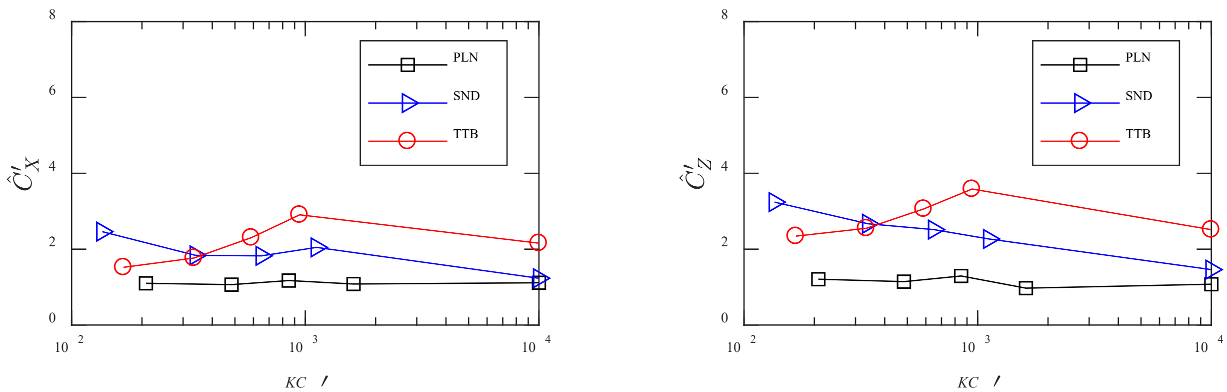

Figure 14. The effect of wall turbulence induced by different seabed roughness conditions on the force coefficients. The steady current results are shown at $KC' = 10^4$.

Figure 15 presents the steady current results $\{\overline{C}_X', \overline{C}_Z'\}$ obtained from tests under different seabed conditions as a function Re_p'. To compare with Jones's (1970) data, the characteristic velocity spanning the cylinder is calculated as $U_{cp} = \sqrt{\frac{1}{D}\int_{z=0}^{D} \overline{u}^2}$, which is identical to that used by Jones (1970). Figure 15 shows that at a constant Re_p', a larger k_s/D leads to greater force coefficients $\{\overline{C}_X', \overline{C}_Z'\}$. In addition, this amplification effect becomes weaker as Re_p' increases. These two behaviours are interpreted as follows.

For a wall-free cylinder, a larger incoming turbulence level leads to an increased force coefficient when the flow around the cylinder is in the lower transition (critical), supercritical and upper transition regimes (Cheung & Melbourne 1983). For a detailed account of the delineation of flow regimes around a wall-free cylinder based on different Reynolds numbers, see Sumer & Fredsøe (2006). For a cylinder approaching the wall, the critical Reynolds number corresponding to each flow regime shifts to smaller values (Yang et al. 2018). For a cylinder experiencing larger incoming turbulence, the critical Reynolds number for each flow regime also decreases. That is, both the wall proximity and incoming turbulence promote the transition of the flow around the cylinder. This knowledge might be helpful for understanding the behaviours shown in Figure 15.

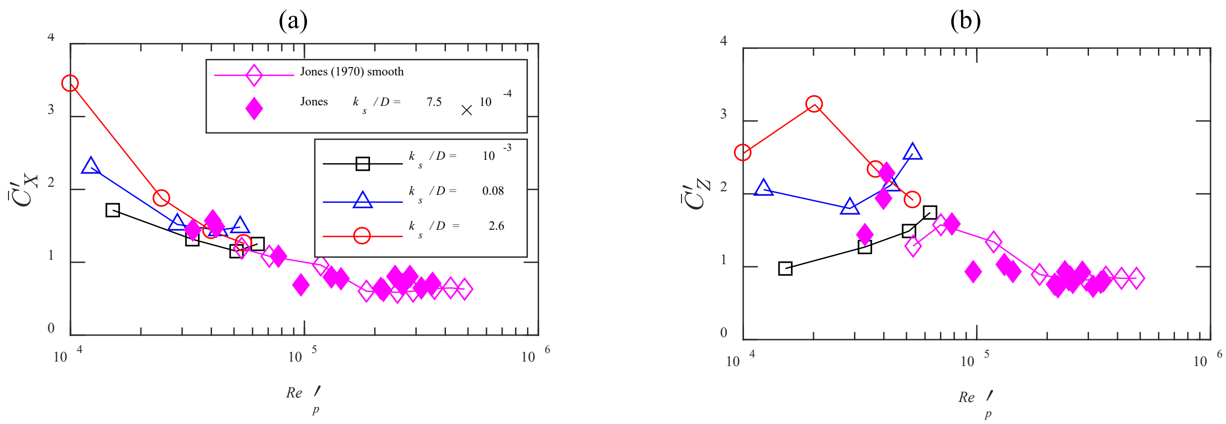

Figure 15. Effect of k_s/D on $\{\overline{C}_X{}', \overline{C}_Z{}'\}$, based on the present steady current results. The characteristic velocity is calculated in the same manner as that in Jones (1970).

The decreasing trend of the mean drag coefficient with increasing $Re_p{}'$, shown in Figure 15, suggests that the boundary layer flow around the cylinder is in a stage between the critical and supercritical regimes, where the boundary layer around the cylinder experiences a transition from laminar to turbulent. Similar to a wall-free cylinder, a larger turbulence level due to a greater k_s/D causes higher force coefficients in the present flow regimes.

As the incoming turbulence (due to wall turbulence) affect the hydrodynamic forces by promoting the transition of the cylinder boundary layer, it is reasonable that the wall turbulence will affect less after the cylinder boundary layer transition completes. This is the reason why the difference in force coefficients induced by wall turbulence (reflected by k_s/D) vanishes as $Re_p{}'$ approaches 10^5. To this end, the results suggest that the wall turbulence affects the forces at $Re_p{}' < 10^5$, where the cylinder boundary layer flow experiences a transition from laminar to turbulent. It worth noting that, for a cylinder placed away from the wall, the incoming turbulence affects both the boundary layer transition around the cylinder and the features of the vortex shedding around the cylinder (e.g., the correlation length); but for a cylinder placed on the wall with all the gaps sealed, i.e., the present setup, the vortex shedding is totally absent (Bearman and Zdravkovich 1978, Sumer & Fredsøe 2006, p23 and p111).

Given the discussions above, the seabed roughness affects the hydrodynamics in the following way. On the one hand, a greater seabed roughness enhances the velocity reduction in the WBLs and therefore leads to smaller forces. On the other hand, a greater seabed roughness leads to stronger wall turbulence that promotes the cylinder boundary layer transition and thus increases the forces. The overall influence of seabed roughness on the force coefficients, either an increase or a decrease, depends on which aspect dominates. In addition, an upper limit of $Re_p{}'$ should exist, above which the wall turbulence negligibly affects the forces, because the cylinder boundary layer can transition to fully turbulent due to the turbulence created by the cylinder itself.

5 Empirical correlations for the force coefficients

A new set of force coefficients, normalized by the freestream velocity amplitude U_w, are proposed based on the PLN results (Figure 10), where k_s/D has a negligible effect (Tang et al. 2018). Meanwhile, a set of correction factors $\{\gamma_x, \gamma_z\}$ are used to consider the effect of seabed roughness on streamwise (horizontal) and transverse (vertical) force coefficients, respectively, based on the SND and TTB results. Furthermore, the deviations due to Re_p are covered by another set of correction factors $\{\zeta_x, \zeta_z\}$, based on all present results. In the parametric range of $20 \le KC \le 2000$, $10^4 \le Re_p \le 10^5$ and $10 \le \beta \le 1000$, the peak force coefficients are formulated as follows:

$$\hat{C}_X = \gamma_x \zeta_x \left(29.35KC^{-0.72} + 0.49\right), \tag{5.1}$$

$$\hat{C}_Z = \gamma_z \zeta_z \left(20.15KC^{-0.64} + 0.50\right). \tag{5.2}$$

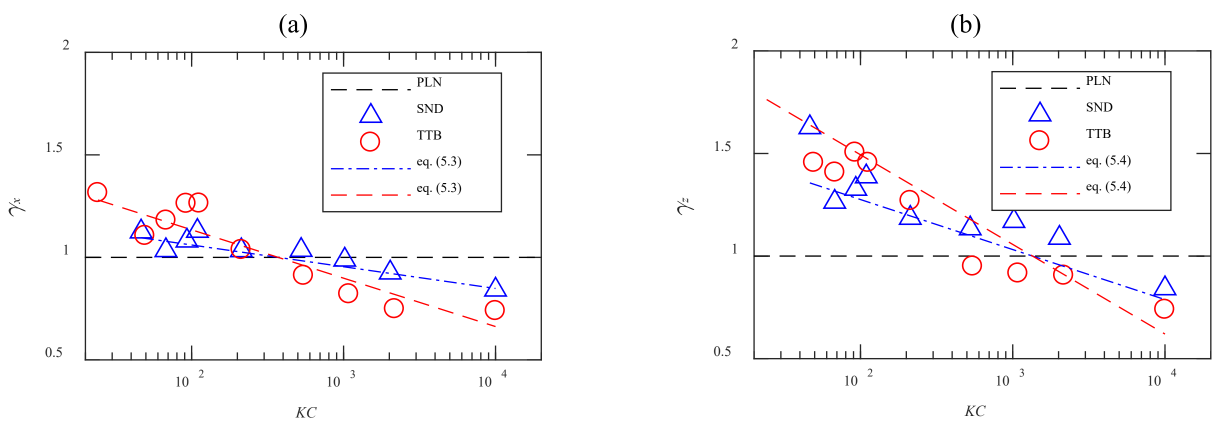

Figure 16. Correction factors to quantify the effect of seabed roughness. Each point in the figure represents the average value in a group of data with different Re_p but identical k_s/D and KC. To facilitate quantification, the current results are given at the KC number of 10^4.

Figure 16 presents the ratios between the results obtained from the rough wall (SND and TTB) and smooth wall (PLN), namely, the correction factors describing the effect of seabed roughness. At the critical KC number where the blue dashed-dotted (red dashed) line intersects the black dashed line (at $KC = 370$ for $\hat{C}_X$ and $KC = 1350$ for $\hat{C}_Z$), the influences of velocity reduction and wall turbulence on $\{\hat{C}_X, \hat{C}_Z\}$ are approximately equal. Empirical formulas for correction factors γ_x and γ_z are given below for the parametric range of $10^{-3} \le k_s/D \le 2.6$:

$$\gamma_x = \left[-0.57\left(\frac{k_s}{D}\right)^{0.06} + 0.37\right] \times \left(\log_{10} KC - 2.57\right) + 1, \tag{5.3}$$

$$\gamma_z = \left[1.66\left(\frac{k_s}{D}\right)^{-0.03} - 2.05\right] \times \left(\log_{10} KC - 3.13\right) + 1. \tag{5.4}$$

Under smooth bed conditions, $k_s/D \le 10^{-3}$, and both γ_x and γ_z should be taken as 1. The fitting results of eqs. (5.3) and (5.4) are shown in Figure 16.

Figure 17 presents the normalized standard deviations of the force coefficients due to different Re_p numbers. The results with the same KC and k_s/D but different Re_p are selected as one group. The standard deviation and the average value are calculated based on these data in each group, and their quotient is denoted as $\mathrm{std}\left(\hat{C}_i\right)/\overline{\hat{C}_i}$. The results of $\mathrm{std}\left(\hat{C}_i\right)/\overline{\hat{C}_i}$ shown in Figure 17 can be approximately represented by the two correction factors ζ_x and ζ_z in the range of $10^4 \le Re_p \le 10^5$:

$$\zeta_x = 1 \pm 0.14, \tag{5.5}$$

$$\zeta_z = 1 \pm 0.25. \tag{5.6}$$

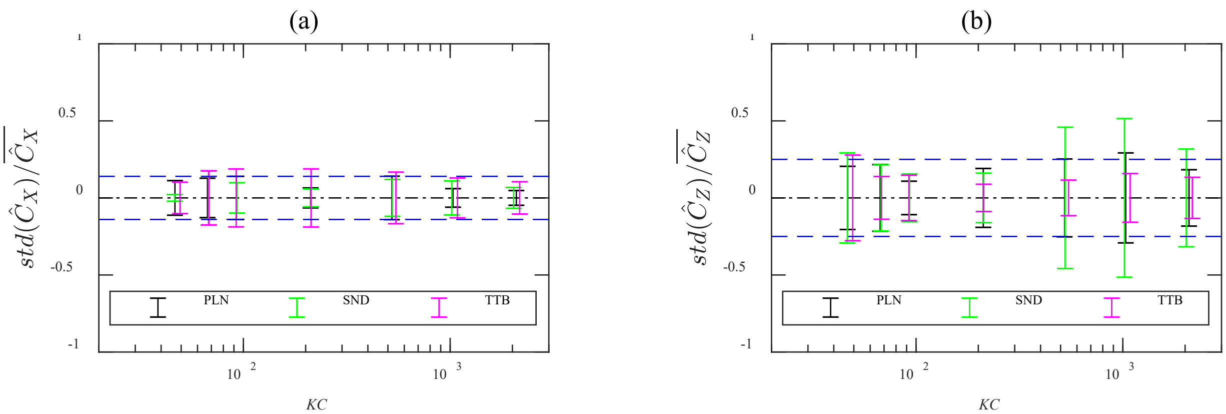

Figure 17. The ratio of the standard deviation over the average value $\mathrm{std}\left(\hat{C}_i\right)/\overline{\hat{C}_i}$ versus KC under the three bottom conditions tested. The blue dashed lines represent the range covered by eqs. (5.5) and (5.6).

Together, these correlations provide a new approach for predicting the peak force coefficients for on-bottom cylinders, capturing the influence of KC and k_s/D for the parameter range relevant to cables and small-diameter pipelines.

An example is illustrated below that employs the present empirical correlations to calculate the lowest specific weight S_g of cables required by the on-bottom stability assessment. The design inputs are described as follows: the cable diameter $D = 0.05$ m; the free stream velocity amplitudes $U_w = 0.5$, 1, 1.5 and 2 m/s; the seabed roughnesses $k_s = 3\times10^{-4}$ m (fine sand), 9×10^{-3} m (gravel), 0.3 m (cobble); wave periods: (a) $T = 20$ s, corresponding to the storm wave whose period is the range of 5 s ~ 30 s, (b) $T = 200$ s, corresponding to a infra-gravity wave or a short-period internal wave which is also commonly considered in the fatigue assessment. Following the absolute lateral static stability method suggested by DNV (2021), the required specific weight is calculated by (Tang et al. 2018)

$$S_g = 1 + \gamma_{sc} \frac{2U_w^2\left(\hat{C}_X + \mu \hat{C}_Z\right)}{\mu \pi g D}, \tag{5.7}$$

where γ_{sc} is a safety parameter, taken as 1.5, and μ is the friction coefficient between the cable and seabed, taken as 0.6. The results of the required S_g calculated with the peak force coefficients suggested by DNV (2021) and the present are compared in Figure 18. For the storm wave, as shown in Figure 18(a), the present force coefficients lead to a reduction in the required specific weight S_g, compared to the S_g based on DNV (2021). This reduction becomes more notable with the increasing KC number and can be up to 25% at KC = 800. But the effect of seabed roughness is not significant under this storm wave condition. For the infra-gravity or short-period internal wave, as shown in Figure 18(b), the result corresponding to the fine sand seabed is 45% smaller than the DNV result at KC = 4000; besides, the cobble seabed can further lead to a 10% reduction at KC = 4000, compared to the fine sand seabed result.

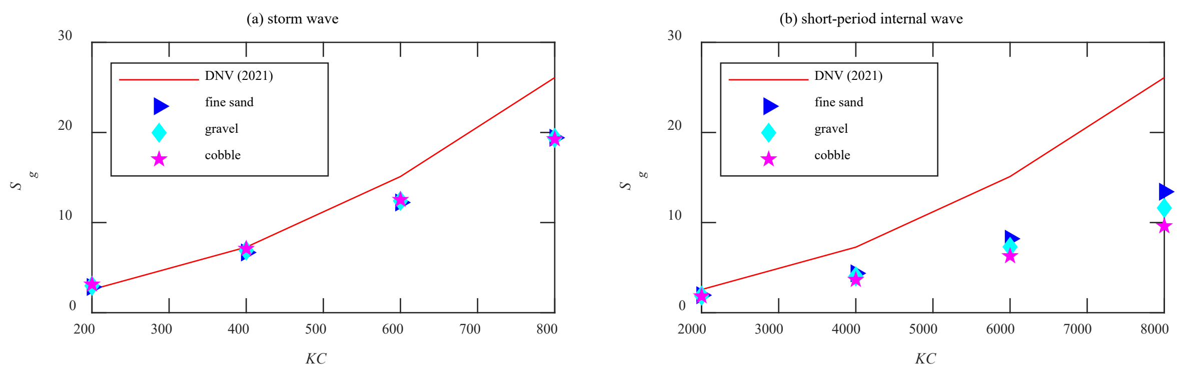

Figure 18. Required specific weight S_g under several combinations of wave conditions and seabed conditions.

6 Conclusion

The hydrodynamic forces on on-bottom small-diameter cables immersed in wave boundary layers (WBLs) are investigated through physical model testing to address a gap in design knowledge. The parametric ranges considered are $20 \leq KC \leq 2000$, $10^4 \leq Re_p \leq 10^5$, $10 \leq \beta \leq 1000$ and $0.001 < k_s/D \leq 2.6$, where KC is the Keulegan–Carpenter number $KC = U_wT/D$, Re_p is the Reynolds number $Re_p = U_wD/\nu$, β is the Stokes number $\beta = Re_p/KC$, and k_s/D is the ratio between the seabed roughness and cable diameter. The following conclusions are drawn.

(1) The present experimental results identified that both the velocity reduction and wall turbulence in the WBLs significantly affect the hydrodynamic forces.

(2) On the smooth plane seabed, the hydrodynamic force coefficients obtained from the present work at large KC numbers (KC > 200) are notably smaller than the recommendations of the design code DNVGL-RP-F109 (2021). This is well demonstrated to be mainly controlled by the velocity

reduction in the WBL.

(3) Under rough seabed conditions, the seabed roughness has two counteracting effects on the hydrodynamic forces. On the one hand, a greater seabed roughness enhances the velocity reduction in the WBLs and therefore leads to smaller hydrodynamic forces. On the other hand, a greater seabed roughness leads to a stronger wall turbulence, which promotes the transition of the cylinder boundary layer flow to turbulent and subsequently increases the forces in the present parameter range. The wall turbulence affects the force coefficients in the range of Reynolds numbers, where the cylinder boundary layer flow experiences the transition from laminar to turbulent. The present results show that the influence of wall turbulence largely diminishes for $Re_p' > 10^5$, where Re_p' is defined with the average velocity across the diameter of the cable.

(4) A general method for quantifying force coefficients under different KC and k_s/D conditions is proposed. This method takes into account the effects of WBL velocity reduction, wall turbulence and Reynolds numbers.

The resulting estimation method for peak hydrodynamic forces provides a basis for a more accurate and economic stability design of on-bottom cables and small-diameter pipelines.

Acknowledgement

The authors would like to acknowledge the support from the National Nature Science Foundation of China through Grants 51890913 and 51979031 and the Australian Research Council (ARC) through Grant LP150100249.

References

van der A, D. A., O'Donoghue, T., Davies, A. G., Ribberink, J. S., 2011. Experimental study of the turbulent boundary layer in acceleration-skewed oscillatory flow. J. Fluid Mech. 684, 251–283.

An, H., Luo, C., Cheng, L., White, D., 2013. A new facility for studying ocean-structure–seabed interactions: the O-Tube. Coast. Eng. 82, 88–101.

Bearman, P. W., Zdravkovch, M. M., 1978. Flow around a circular cylinder near a plane boundary. J. Fluid Mech. 89(1), 33–48.

Cheng, L., An, H., Draper, S., White D., 2016. Effect of wave boundary layer on hydrodynamic forces on small diameter pipelines. Ocean Eng. 125, 26–30.

Cheung, J. C. K., Melbourne, W. H., 1983. Turbulence effects on some aerodynamic parameters of a circular cylinder at supercritical Reynolds number. J. Wind Eng. Ind. Aerodyn. 14, 399–410.

DHI report, 1986. Hydrodynamic forces on pipelines, Model tests. American Gas Association, PR-170-185, Danish Hydraulic Institute.

Dixen, M., Hatipoglu, F., Sumer, B. M., Fredsøe, J., 2008. Wave boundary layer over a stone-covered bed. Coast. Eng. 55(1), 1–20.

DNV-RP-F109, 2021. On-bottom stability design of submarine pipelines. Recommended Practice, Det Norske Veritas AS.

Fredsøe, J., Sumer, B. M., Andersen, J., Hansen, E. A., 1985. Transverse vibrations of a cylinder very close to a plane wall. Proc. 4th Symp. on Offshore Mechanics and Arctic Engineering, OMAE, Dallas, TX, 1, 601–609. (Also: Trans. of the ASME, J. Offshore Mechanics and Arctic Engineering, 109, 52–60)

Gaudin, C., White, D. J., Boylan, N., Breen, J., Brown, T., De Catania, S., Hortin, P., 2009. A wireless high-speed data acquisition system for geotechnical centrifuge model testing. Meas. Sci. Technol. 20(9), 095709.

Gerlach, C. R., Dodge, F. T., 1970. An engineering approach to tube flow-induced vibrations. Proc. Conf. on Flow-Induced Vibrations in Reactor system components, Argonne National Laboratory, pp. 205–225.

Griffiths, T., Draper, S., White, D., Cheng, L., An, H., Fogliani, A., 2018. Improved stability design of subsea pipelines on mobile seabeds: Learnings from the stablepipe JIP. Proc. 37th Int. Conf. on Ocean, Offshore & Arctic Engineering, Madrid, OMAE2018-77217.

Griffiths, T., Teng, Y., Cheng, L., An, H., Draper, S., Mohr, H., Fogliani, A., Mariani, A., White, D., 2019. Hydrodynamic forces on near-bed small diameter cables and pipelines in currents, waves and combined flow. Proc. 38th Int. Conf. on Ocean, Offshore & Arctic Engineering, Glasgow, OMAE2019-95557.

Jensen, B. L., Sumer, B. M., Fredsøe, J., 1989. Turbulent oscillatory boundary layers at high Reynolds numbers. J. Fluid Mech. 206, 265–297.

Jones, W., 1970. Forces on a transverse circular cylinder in the turbulent boundary layer of a steady Flow. Ph. D Thesis, Rice University.

Jonsson, I. G., Carlsen, N. A., 1976. Experimental and theoretical investigations in an oscillatory turbulent boundary layer. J. Hydraul. Res. 14(1), 45–60.

Kamphuis, J. W., 1975. Friction factor under oscillatory waves. J. Waterw. Port, Coast. Ocean Eng. Div. ASCE 101(WW2), 135–144.

Leckie, S. H. F., Draper, S., White, D. J., Cheng, L., Fogliani, A., 2015. Lifelong embedment and spanning of a pipeline on a mobile seabed. Coast. Eng. 95, 130–146.

Milne, I. A., Sharma, R. N., Flay, R. G., Bickerton, S., 2013a. Characteristics of turbulence in the flow at tidal stream power site. Phil. Trans. R. Soc. A, 371(1985), 20120196.

Milne, I., 2013b. An experimental investigation of turbulence and unsteady loading on tidal turbines. Ph. D. thesis, University of Auckland.

Milne, I. A., Graham, J. M. R., Coles, D. S., 2021. On the scaling of turbulence in a high Reynolds number tidal flow. J. Fluid Mech. 915, A104.

Mercier, P., Thiébaut, M., Guillou, S., Maisondieu, C., Poizot, E., Pieterse, A., Thiébot, J., Filipot, J., Grondeau, M., 2021. Turbulence measurements: An assessment of acoustic doppler current profiler accuracy in rough environment. Ocean Eng. 226, 108819.

Sarpkaya, T., Rajabi, F., 1979. Hydrodynamic drag on bottom-mounted smooth and rough cylinders in periodic flow. Proc. 11th Annual Offshore Technology Conf. Houston, TX, Paper OTC 2898, 3, 161–166.

Schewe, G., 1983. On the force fluctuations acting on a circular cylinder in crossflow from subcritical up to transcritical Reynolds numbers. J. Fluid Mech. 133, 265–285.

Sleath, J. F. A., 1987. Turbulent oscillatory flow over rough beds. J. Fluid Mech. 182, 369–409.

Sumer, B. M., Jensen, B. L., Fredsøe, J., 1991. Effect of a plane boundary on oscillatory flow around a circular cylinder. J. Fluid Mech. 225, 271–300.

Sumer, B. M., Fredsøe, J., 2006. *Hydrodynamics around cylindrical structures.* World Scientific.

Tang, G., Cheng, L., Lu, L., Teng, Y., Zhao, M., An, H., 2018. Effect of oscillatory boundary layer on hydrodynamic forces on pipelines. Coast. Eng. 140, 114–123.

Teng, Y., Lu, L., Cheng, L., Tang, G., Tong, F., 2021. A modified defect function for wave boundary layers. Coast. Eng. 171, 104050.

Thielicke, W., Stamhuis, E. J., 2014a. PIVlab - Towards User-friendly, Affordable and Accurate Digital Particle Image Velocimetry in MATLAB. Journal of Open Research Software, 2(1): e30.

Thielicke, W., Stamhuis, E. J., 2014b. PIVlab - Time-Resolved Digital Particle Image Velocimetry Tool for MATLAB (version: 1.50).

Thielicke, W., 2014. The Flapping Flight of Birds - Analysis and Application. Ph. D thesis, Rijksuniversiteit Groningen.

Westergaard, C. H., Madsen, B. B., Marassi, M., Tomasini, E. P., 2003. Accuracy of PIV signals in theory and practice. In 5th Int. Symp. on Particle Image Velocimetry, Busan, paper 3301.

White, D. J., Draper, S., Cheng, L., An, H., Mohr, H., Leckie, S., 2014. Ocean-structure-seabed interaction: O-tube modelling of pipeline stability. Aust. Geomech. J. 49(4), 157–164.

Yamamoto, T., Nath, J. H., 1976. High Reynolds number oscillating flow by cylinders. Proc. 15th Int. Conf. on Coastal Eng. III, 2321–2340.

Yang, F., An, H., Cheng, L., 2018. Drag crisis of a circular cylinder near a plane boundary. Ocean Eng. 154, 133–142.

Yuan, J., Madsen, O. S., 2014. Experimental study of turbulent oscillatory boundary layers in an oscillating water tunnel. Coast. Eng. 89, 63–84.

Zhang, Q., Draper, S., Cheng, L., An, H., 2017. Time scale of local scour around pipelines in current, waves and combined waves and current. J. Hydraul. Eng. 143(4), art. no. 04016093.